Article

Multi-Band Frequency Window for Time-Frequency Fault Diagnosis of Induction Machines

Jordi Burriel-Valencia, Ruben Puche-Panadero, Javier Martinez-Roman, Angel Sapena-Bano*, Martin Riera-Guasp, Manuel Pineda-Sanchez

The authors are with the Institute for Energy Engineering, Universitat Politècnica de València, Camino de Vera s/n, 46022, Valencia, Spain; jorburva@die.upv.es, rupucpa@die.upv.es, jmroman@die.upv.es, asapena@die.upv.es, mriera@die.upv.es, mpineda@die.upv.es

* Correspondence: asapena@die.upv.es; Tel.: +34-96-3877597

† All the authors contributed equally to this work.

Abstract: Induction machines drive many industrial processes, and their unexpected failure can cause heavy production losses. The analysis of the current spectrum can identify online the characteristic fault signatures at an early stage, avoiding unexpected breakdowns. Nevertheless, frequency domain analysis requires stable working conditions, which is not the case for wind generators, motors driving varying loads, etc. In these cases an analysis in the time-frequency domain -such as a spectrogram- is required for detecting faults signatures. The spectrogram is built using the short frequency Fourier transform, but its resolution depends critically on the time window used to generate it: short windows provide good time resolution, but poor frequency resolution, just the opposite than long windows. Therefore, the window must be adapted at each time to the shape of the expected fault harmonics, by highly skilled maintenance personnel. In this paper, this problem is solved with the design of a new multi-band window, which generates simultaneously many different narrow-band current spectrograms, and combines them into as single, high resolution one, without the need of manual adjustments. The proposed method is validated with the diagnosis of bar breakages during the start-up of a commercial induction motor.

Keywords: fault diagnosis; induction motors; wind energy generation; fourier transforms; spectral analysis; spectrogram; transient regime

1. Introduction

Induction machines (IMs) are a key component of many industrial processes, either as motors or as generators, such as double fed induction generators (DFIGs) used for wind energy generation. Their reliability ensures the continuity of the production processes, but they are subjected to eventual failures (broken bars, bearing faults, eccentricity, turn to turn or phase to ground short-circuits, etc.), which may cause unexpected breakdowns and high economic losses. A way to reduce these risks is the continuous monitoring of the machine's condition, in order to detect the presence of a fault at an early stage, when corrective measures can be implemented or maintenance works scheduled. Diverse quantities have been proposed in the technical literature for implementing condition based maintenance systems (CBMS) [1,2], such as the analysis of the stator currents [3–7], machine vibrations [8–10], fluxes [11,12], thermal images [13], or acoustic signals [14,15]. These techniques have been applied to detect different types of faults not only of the IM, such as stator inter-turn short circuits [11,16], broken bars [17,18], rotor asymmetries [19], eccentricity [20], bearing faults [6,21], but also of the inverter drive [3] or the mechanical coupling to the load, as gearboxes and pulleys [3,22].

Table 1. Characteristic Frequencies of Different Types of IM Faults

Type of fault	Fault Harmonics Frequency	
Shorted coils	$f_1\left(k \pm n\frac{1-s}{p}\right)$	$k = 1,3,5\ldots$ $n = 1,2,3,\ldots$
Rotor asymmetries	$f_1\left((1-s)\frac{k}{p} \pm s\right)$	$\frac{k}{p} = 1,3,5\ldots$
Mixed eccentricity	$\lvert f_1 \pm k f_r \rvert$	$k = 1,2,3\ldots$
Bearing (outer race)	$\frac{N_b}{2} f_r \left[1 - \frac{D_b \cos(\beta)}{D_c}\right]$	
Bearing (inner race)	$\frac{N_b}{2} f_r \left[1 + \frac{D_b \cos(\beta)}{D_c}\right]$	
Bearing (balls)	$\frac{D_c f_r}{2D_b}\left[1 - \left(\frac{D_b \cos(\beta)}{D_c}\right)^2\right]$	

A diagnostic technique that has gained a widespread interest in recent years is the motor current signature analysis (MCSA) [23–26], which is based on the detection of the characteristic fault signatures that each type of fault impress in the current spectrum. It is a non-invasive method, which can be applied on line without disturbing the normal operation of the machine; it requires, in its more basic implementation, just a current sensor for acquiring the current signal and a fast Fourier transform (FFT) for generating its spectrum; and it can detect a wide variety of machine faults through their spectral signatures, because each type of fault generate a specific set of fault frequencies, as shown in Table 1 [27], where f_1 stands for the fundamental component frequency, p is the number of pole pairs, s is the machine slip, f_r is the rotational frequency of the IM rotor, N_b is the number of balls of the bearings, D_b if the bearing diameter, D_c is the pitch or cage diameter, and β is the contact angle.

Nevertheless, the use of the current spectrum as signal processing tool in MCSA limits its field of application to machines working in stationary conditions, which is not the case of industrial processes with varying load or speed conditions, or also of wind generators operating under variable wind regimes. In these cases, the fault frequencies shown in Table 1 become random time functions, and the fault harmonics do not produce isolated spectral lines in the current spectrum, which blurs their characteristic signatures.

To extend MCSA to the fault diagnosis of IM working in transient regime, advanced time-frequency (TF) transforms of the current are needed, so that the transient fault signatures can be identified in a joint TF domain. These transforms can be lineal, such as the short-time Fourier transform (STFT) [28–30], the short-frequency Fourier transform (SFFT) [31], and the wavelet transform (WT)[32], or quadratic, such as the Wigner-Ville distribution (WVD) [33], or the ambiguity function [34]. Quadratic TF transforms can achieve optimal resolution for mono-component chirp signals, but in case of multi-component ones, they produce cross-terms artifacts that pollute the TF representation of the current, making it difficult the correct identification of the fault harmonics. On the contrary, linear TF transforms are free from cross-terms artifacts. The STFT representation, the spectrogram, and the WVD representation, are built by multiplying the current signal with an analysing window at each time instant, and performing the FT of the resultant signal. In the case of the STFT, this window has a constant shape, which makes it difficult to obtain a good resolution both in time and in frequency: a short window gives a good time resolution, but a poor frequency resolution; on the contrary, a long window gives a good frequency resolution, but a poor time resolution. The WT solves this issue by performing a multi-resolution analysis, using different windows at different frequency bands: long windows for the lower frequency bands, and short windows for the higher frequency bands. But this approach makes the application of the WT much more complex than the FT, and distorts the TF signature of the fault harmonics.

Diverse solutions to this problem have been proposed recently, in order to built a current's spectrogram with enough resolution for being used as an IM fault diagnosis tool. One of them is to adapt the shape of the analyzing window in the TF domain to the expected shape of the fault harmonics, either using a single window, as in [35], or using different window shapes for different sections of the current signal, as in [36]. This approach requires a deep a priori knowledge of the time evolution of the fault harmonics in the current signal, which requires highly skilled maintenance personnel for implementing it, and difficult its application in automated diagnostic systems. Other approach apply to the spectrogram a post-processing based on reassignment [37] or synchrosqueezing [9,38] techniques, so improving its sharpness, but these techniques add a considerable computational burden to the process of building the current spectrogram, departing from the simplicity of the STFT. Another alternative for obtaining an improved spectrogram is the Matching Pursuit approach [39]. This method is based on calculating a series of spectrograms, using a set of different windows designated as "dictionary" [40], which has to be previously built. Then, combining spectrograms corresponding to each window of the dictionary through a pre-defined algorithm, obtains the final spectrogram, which is considered the optimum one. This method has several drawbacks, such as the need of building an extensive dictionary, with a great amount of different windows for obtaining a good resolution spectrogram. This implies to calculate a huge quantity of spectrograms and thus consuming a vast quantity of time and computational resources

In this paper, a novel approach (up to the best of the authors' knowledge) is proposed to obtain a high-resolution current spectrogram, useful for fault diagnostic purposes, with the simplicity of a single STFT. It is based on

1. Performing the STFT with a wide range of windows with different lengths, and selecting, for each point in the TF domain, the best result obtained at that point among the complete set of windows.
2. Instead of running a separate STFT for each of the windows used in the analysis, a single, multi-band window is built by stacking all the desired analysing windows in consecutive frequency bands. This approach obtains in parallel the spectrograms corresponding to several hundreds of different analysis windows with the computing cost of a single one, which makes it suitable for fast, online diagnostic systems in transient regime.

The structure of the paper is as follows. In Section 2 the generation of the spectrogram with Gaussian windows shifted in the frequency domain is analyzed, and in Section 3 it is used for the theoretical and practical explanation of the proposed method. In Section 4, it is validated with the analysis of the start-up current of a high rated power, medium voltage squirrel cage induction motor, with broken bars. Section 5 presents the conclusions of this work.

2. Time-Frequency Analysis of the Machine's Current via STFT with a Multi-Band Window

To highlight the spectral content of a time-varying current signal, which may contain the characteristic fault harmonics given in Table 1, it is necessary to generate a representation of the current signal in the join TF domain. Among the diverse transforms available to this end (STFT, SFFT, WT, WVD, ambiguity function, etc.), the STFT has been selected in this work, because it is a linear transform, without cross-terms artifacts, and is computationally very effective, which makes it suitable for being implemented in low-cost, low-power embedded devices for on-line CBM systems.

In this Section, the traditional STFT analysis of the stator current using a Gaussian window will be first reviewed, and after the proposed method using a multi-band frequency window will be presented and compared with the traditional one.

2.1. Spectrogram of Machine's Current

The STFT of a current signal $i(t)$ is a linear TF transform that is able to generate a joint TF representation of the current, the spectrogram, through the following steps:

1. For each instant τ, the current signal is multiplied element by element by the conjugate of a suitable time window centered at τ, $h(t-\tau)$

$$i_\tau(t) = i(t)h(t-\tau)^* \tag{1}$$

that emphasizes the content of the current signal at time τ, and attenuates it at other times

$$i_\tau(t) = \begin{cases} i(t), & \text{if } t \text{ is close to } \tau \\ 0, & \text{if } t \text{ is far from } \tau \end{cases} \tag{2}$$

2. The Fourier transform if applied to the time-windowed signal $i_\tau(t)$, which gives the frequency content of the current signal $i(t)$ around time τ

$$\begin{aligned} I_\tau(\omega) &= \tfrac{1}{\sqrt{2\pi}} \int e^{-j\omega t} i_\tau(t) dt \\ &= \tfrac{1}{\sqrt{2\pi}} \int e^{-j\omega t} i(t) h(t-\tau)^* dt \end{aligned} \tag{3}$$

where $\omega = 2\pi f$, and f stands for the frequency, in Hz.

3. The energy density spectrum at time τ is obtained as

$$I_{SP}(\tau,\omega) = |I_\tau(\omega)|^2 = \left| \frac{1}{\sqrt{2\pi}} \int e^{-j\omega t} i(t) h(t-\tau)^* dt \right|^2 \tag{4}$$

For each instant τ the STFT generates a different energy spectral density $I_{SP}(\tau,\omega)$, and the total set of these spectra constitutes the current spectrogram. A critical issue for obtaining a high resolution spectrogram of the current signal is the selection of the window $h(t)$ in (4). To obtain a high resolution of the energy content of the current signal in the joint TF domain, it is necessary to use a window with a high concentration of energy in the TF plane, but such energy concentration is limited by the Heisenberg's uncertainty principle : a short time window gives a good time resolution, but a poor frequency resolution, and, on the contrary, a long time window gives a good frequency resolution, but a poor time resolution. The window that can achieve the highest energy concentration in the joint TF domain is the Gaussian window [35], given in the time domain by

$$g(t) = \left(\frac{\alpha}{\pi}\right)^{1/4} e^{\frac{-\alpha}{2}t^2} \tag{5}$$

and in the frequency domain by

$$G(\omega) = \left(\frac{1}{\alpha\pi}\right)^{1/4} e^{-\frac{1}{2\alpha}\omega^2} \tag{6}$$

The standard deviation of the Gaussian window in the time domain (5) is $\sigma_t^2 = 1/(2\alpha)$, and in the frequency domain (6) is $\sigma_\omega^2 = \alpha/2$. Therefore, for the Gaussian window, the product of its duration σ_t and its bandwidth σ_ω gives [41]

$$\sigma_t \sigma_\omega = 1/2 \tag{7}$$

The Heisenberg's uncertainty principle states that one cannot construct any signal whose duration σ_t and bandwidth σ_ω are, both, arbitrarily small, because

$$\sigma_t \sigma_\omega \geq 1/2 \tag{8}$$

In this way, the Gaussian window has a duration-bandwidth product (7) that reaches the minimum value (i.e, the highest concentration in the joint TF plane) that can be achieved under the uncertainty principle (8).

The parameter α in (5) and in (6) is the only one that defines the shape of the Gaussian window. A low value of α gives a long window with a narrow bandwidth, while a high value of α gives a short window, with a wide bandwidth. This parameter must be tuned to the current signal to be analyzed with the STFT. As detailed in [35], the optimal Gaussian window to build the spectrogram of a given current signal is the one that has the maximum overlap with the current in the TF domain. That is, the optimal parameter α is the one whose height/width ratio $\sigma_\omega/\sigma_t = \alpha$ best approximates the slope of the current signal in the TF domain. Unfortunately, the slope of the fault harmonics in an IM in transient regime is not a constant value, because in this regime the slip and the rotational frequency in Table 1 are time-varying quantities, as well as the fault frequencies that depend on them. Besides, different components of the current signal may have different slopes (such as the fundamental component and the fault harmonics). These facts preclude the use of a single, optimal Gaussian windows for building a high resolution diagnostic spectrogram of the IM current.

2.2. Frequency Shifting of the Gaussian Analysing Window

If the Gaussian window (5) is used as the analysing window to build the energy density spectrum, then (4) becomes

$$I_{SP}(\tau,\omega) = |I_\tau(\omega)|^2 = \left|\frac{1}{\sqrt{2\pi}}\int e^{-j\omega t} i(t) g(t-\tau)^* dt\right|^2 \tag{9}$$

The Gaussian window (5) is a real valued function. If it shifted in the frequency domain by a frequency f_k, corresponding to an angular frequency $\omega_k = 2\pi f_k$, then (5) becomes a complex-valued function

$$g_k(t) = g(t)e^{j\omega_k} = \left(\frac{\alpha}{\pi}\right)^{1/4} e^{\frac{-\alpha}{2}t^2} e^{j\omega_k} \tag{10}$$

Replacing (10) in (9) gives

$$I_{SP}(\tau,\omega) = |I_\tau(\omega)|^2 = \left|\frac{1}{\sqrt{2\pi}}\int e^{-j\omega t} i(t) g(t-\tau)^* e^{-j\omega_k} dt\right|^2 \tag{11}$$

that is,

$$I_{SP}(\tau,\omega) = |I_\tau(\omega)|^2 = \left|\frac{1}{\sqrt{2\pi}}\int e^{-j(\omega+\omega_k)t} i(t) g(t-\tau)^* dt\right|^2 \tag{12}$$

and, making the change of variable $\omega' = \omega + \omega_k$, (12) can be expressed as

$$I_{SP}(\tau,\omega'-\omega_k) = |I_\tau(\omega'-\omega_k)|^2 = \left|\frac{1}{\sqrt{2\pi}}\int e^{-j\omega' t} i(t) g(t-\tau) dt\right|^2 \tag{13}$$

Therefore, as the shift ω_k of the Gaussian analysis window changes, the frequencies of the entire corresponding spectrogram (13) suffer the same ω_k shift, at each time τ.

3. Proposed Multi-Band Analysing Window

A possible approach for obtaining a high-resolution spectrogram of a current signals with components of different slopes in the TF domain could be a variant of the Matching Pursuit approach, using as dictionary a set of Gaussian functions with different values of α. In this way, a batch of

spectrograms, each one with a different value α for the Gaussian window (5) would be generated. In a second stage, for each point in the TF domain, the best value obtained among the whole set of spectrograms would be selected, giving the best approximation to the ideal TF representation of the current signal.

The drawback of this technique is the high amount of resources that it requires. For each possible value of α, in a given range, a full spectrogram must be built, which is a time-consuming operation, and, also, it must be stored, which implies high memory resources. Afterwards, a processing algorithm must be applied to each point of all the spectrograms to combine them. These requirements make this technique unsuitable for being deployed with on-line, low power embedded devices.

On the contrary, the novel technique presented in this paper can achieve the same results at roughly the cost of a single STFT, in terms of speed and storage requirements, even with the use of several hundreds of Gaussian windows with different values of α. It is based on a particular feature of the IM faults presented in Table 1: in most industrial IMs, the fault harmonics with the highest amplitudes are those with an index $k = 1$, and they are located in a narrow, low frequency band with a bandwidth f_b (normally of one or two hundreds of Hz). Nevertheless, the current signal is acquired normally using high frequencies rates, from 5 or 10 kHz up to 100 kHz and more. This implies that, when performing the FT of the windowed current signal, at each stage of the STFT process, only the values within the narrow band $[0 - f_b]$ of diagnostic interest are kept, and the rest of the spectrogram values are discarded, what represents a waste of computing resources.

The proposed method addresses this problem, filling the whole spectrogram with useful diagnostic contents. It relies on frequency shifting the Gaussian analysing window, as in sub-section 2.2, (13). If the current signal is low-pass filtered with a cut-off frequency f_b (using, for example, a frequency filter as in [42]), then its spectrogram, built with a Gaussian window (5), will be non-zero only in the frequency band of diagnostic interest $[0 - f_b]$. But, if the Gaussian window is shifted to a frequency $f_k = f_b$ in (10), then the spectrogram of filtered current signal will appear in the frequency band $[f_b - 2f_b]$ (and will be zero outside this band). If the α parameters of both Gaussian windows (the shifted and the non-shifted one) are equal, the same spectral information will appear in both frequency bands. But, if the shifted Gaussian window has a different value of α, then the spectrograms in the frequency bands $[0 - f_b]$ and $[f_b - 2f_b]$ will be different, each one corresponding to a different value of the parameter α.

What is proposed in this paper is to extend this feature, using, instead of two frequency bands, a partition of the whole spectrogram in N_g adjacent bands, each one with a frequency width equal to f_b; and to use a set of N_g Gaussian windows, with different values of α (α_k, $k = 0 \dots N_g - 1$), and with increasing shifting frequencies ($f_k = kf_b$, $k = 0 \dots N_g - 1$), for filling each of these frequency bands. This can be achieved in a single run of the FFT if, using the superposition principle, all these N_g, frequency shifted, Gaussian windows are summed in the time domain, giving a single time window. The use of this new, multi-band window, in (4) gives a single spectrogram with N_g adjacent bands, each one corresponding to the analysis of the current signal with a different parameter α_k for the Gaussian window.

For a given sampling frequency f_s, and a frequency band of interest f_b, the total number N_g of adjacent frequency bands that can be used is equal to

$$N_g = f_s / f_b \tag{14}$$

The proposed multi-band window is built, using (10), as

$$gm(t) = \sum_{k=0}^{N_g-1} \left(\frac{\alpha_k}{\pi}\right)^{1/4} e^{-\frac{\alpha_k}{2}t^2} e^{jk2\pi f_b} \tag{15}$$

As an example, a multi-band window (15) has been built using $N_g = 10$ different Gaussian windows with values of α in (5) spanning linearly the range [$\alpha_{min} = 1$ - $\alpha_{max} = 700$], with a step equal to $\Delta\alpha = (\alpha_{max} - \alpha_{min})/(N_g - 1)$, as

$$gm(t) = \sum_{k=0}^{N_g-1} \left(\frac{\alpha_{min} + k\Delta\alpha}{\pi}\right)^{1/4} e^{-\frac{\alpha_{min}+k\Delta\alpha}{2}t^2} e^{jk2\pi f_b t}. \quad (16)$$

The multi-band window (16) is displayed in Fig. 1, which shows the real (Fig. 1.top) and the imaginary part (Fig. 1.middle) of the window, as well as its spectrum (Fig. 1.bottom). Fig. 2 shows the spectrogram of the window in the joint TF domain, with all the individual Gaussian atoms stacked in adjacent frequency bands.

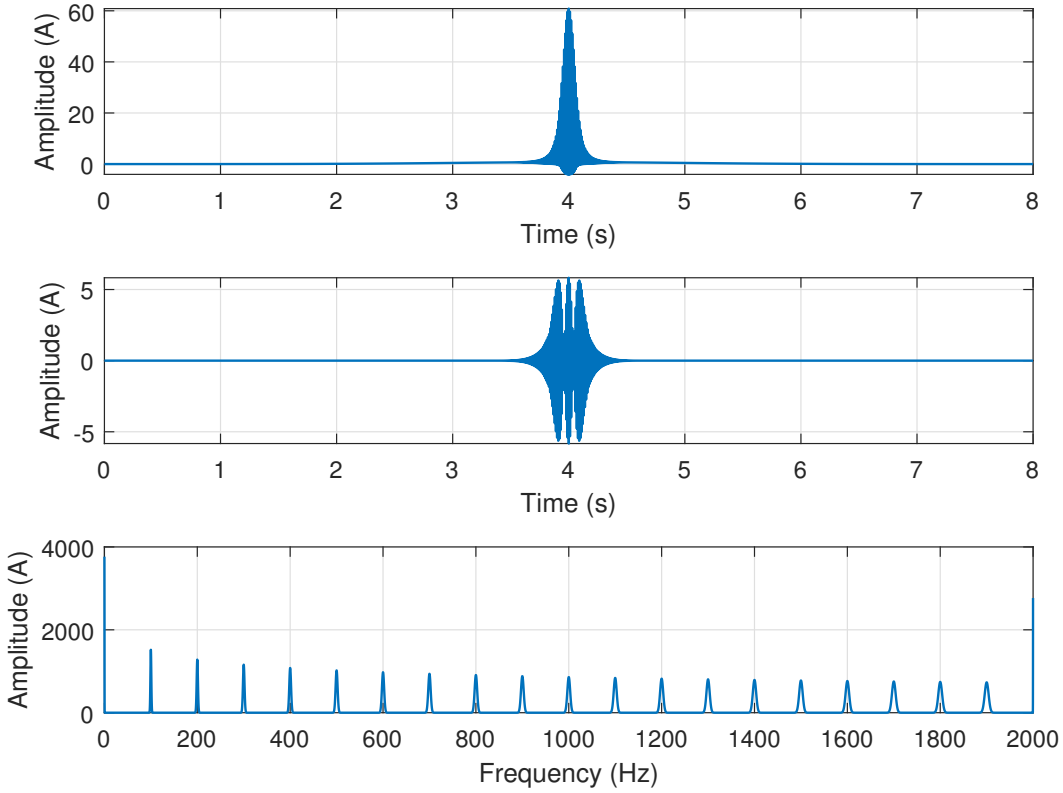

Figure 1. Multi-band window designed in Section 3 in the time domain (real part, top, imaginary part, middle), and in the frequency domain (bottom). This windows contains 20 Gaussian windows, located in 20 adjacent frequency bands of 100 Hz, spanning linearly the range [$\alpha = 1$ - $\alpha = 700$].

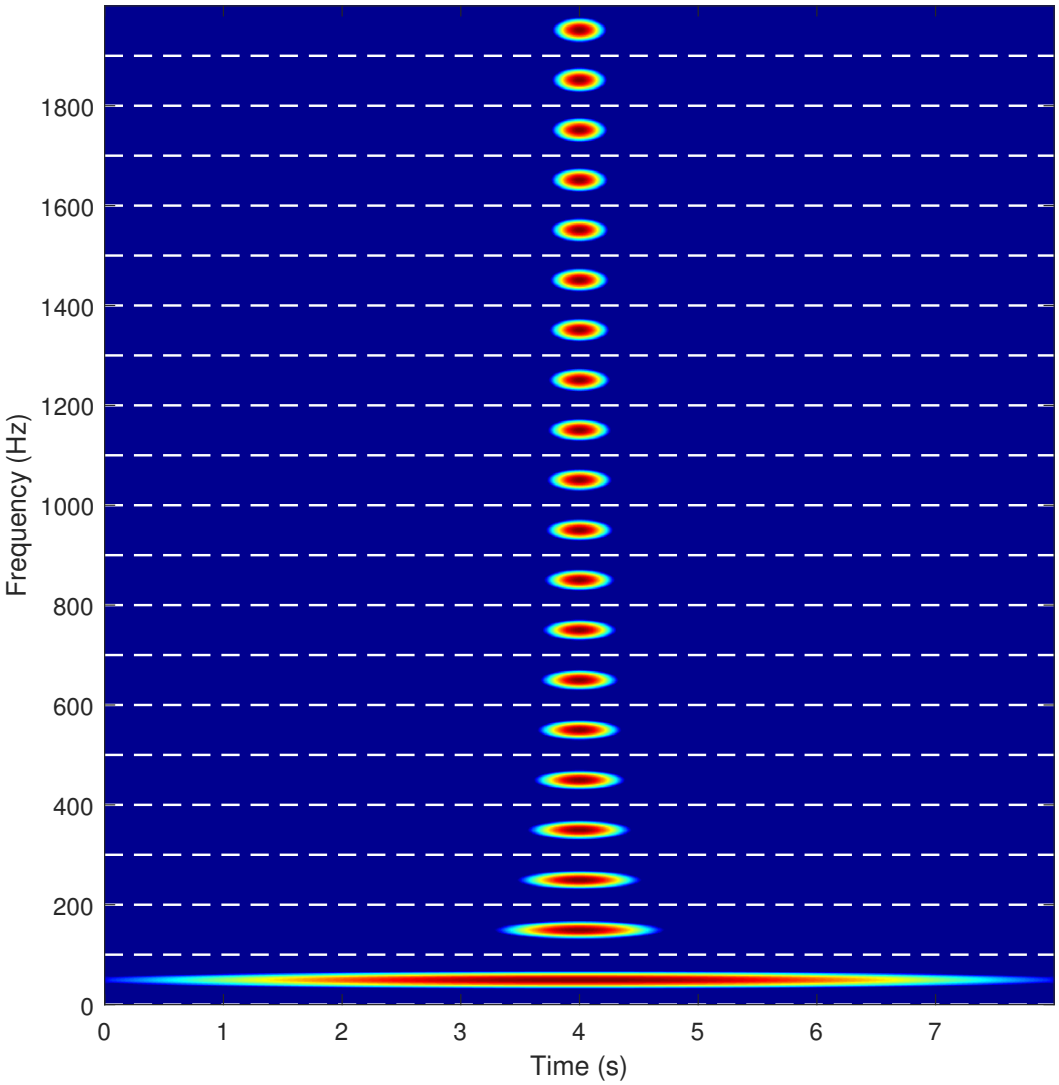

Figure 2. Atoms of the multi-band window designed in Section 3 in the joint time-frequency domain. This windows contains 20 Gaussian windows, located in 20 adjacent frequency bands of 100 Hz, spanning linearly the range from $\alpha = 1$ (bottom) up to $\alpha = 700$ (top).

3.1. Steps for Applying the Proposed Multi-Band Window

In this sub-section the process for applying the concept of multi-band window to a given current signal $i(t)$ is explained, using a synthetic current signal $i(t)$ with a sinusoidal component of 50 Hz, and a linear chirp with a frequency slope of 1 Hz/s, starting at -50 Hz. It has been built with a duration of 50 s, using a frequency sampling rate of 200 Hz (Fig. 3),

$$i(t) = \cos(2\pi 50t) + 0.05\cos(2\pi(-50t + t^2)). \tag{17}$$

Preprints (www.preprints.org) | NOT PEER-REVIEWED | Posted: 5 August 2019 doi:10.20944/preprints201908.0039.v1

Peer-reviewed version available at Energies 2019, 12, 3361; doi:10.3390/en12173361

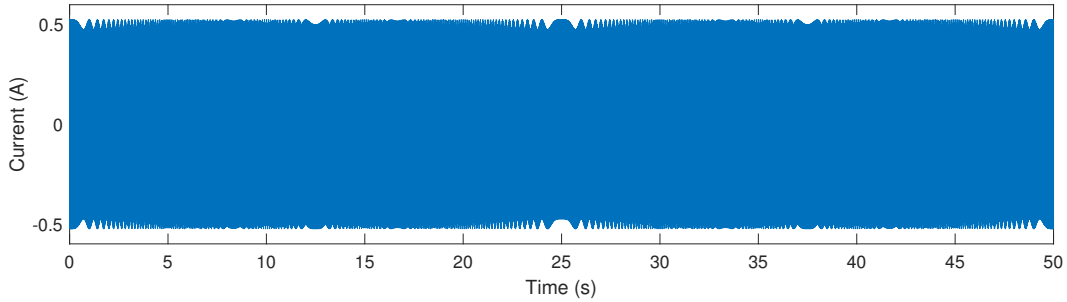

Figure 3. Synthetic current signal (17) used for illustrating the application of the proposed method.

The steps for analysing the current signal (17) using the proposed multi-band windows are the following ones:

1. The analysis window (15) is built:
   - first, the bandwidth of diagnostic interest [0-f_b] is established ([0-]100 Hz] in this case), which gives the maximum number of elementary Gaussian windows from (14) ($Ng = 200/100 = 2$). The current signal is low-pass filtered with a cut-off frequency equal to f_b. In this work, a spectral filter which zeroes all the spectrum bins with a frequency greater than f_b has been used, as in [42].
   - second, the parameters α_k of each of these windows in (15) must be selected. For the simple signal (17), only two values of α are used, $\alpha_0 = 1$ (a long window), and $\alpha_1 = 12.6$, tailored to the chirp component according to [35].

   The resulting multi-band window expression, applying (15), is

$$gm(t) = \left(\frac{1}{\pi}\right)^{1/4} e^{-t^2/2} + \left(\frac{12.6}{\pi}\right)^{1/4} e^{-12.6t^2/2} e^{j2\pi 100t} \tag{18}$$

   This window is plotted in Fig. 4, in the time and frequency domains.

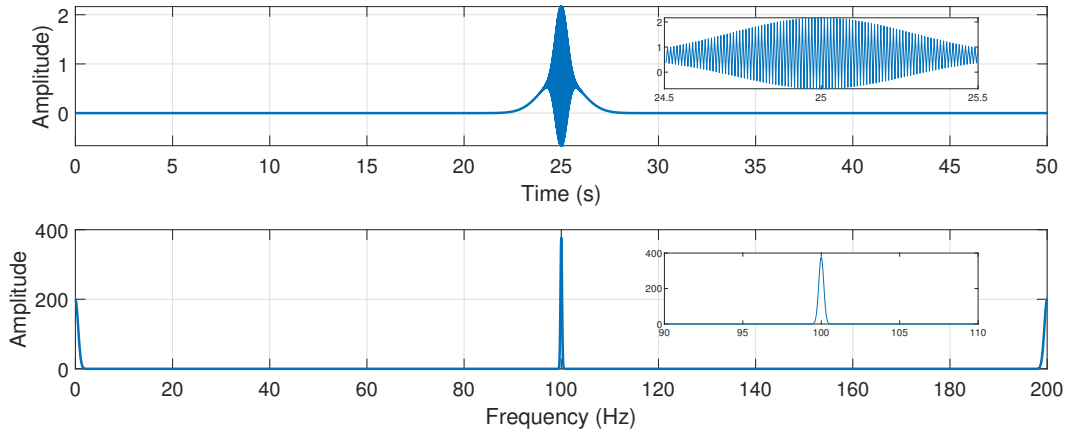

Figure 4. Multi-band window (15) in the time domain (top), and in the frequency domain (bottom). This windows contains 2 Gaussian windows, in 2 adjacent frequency bands of 100 Hz, one with $\alpha = 1$ and the other one with $\alpha = 12.6$.

2. The spectrogram of the current signal (17) is built, using the multi-band window (18) as sliding window (Fig. 5). It shows two elementary spectrograms in adjacent TF regions, obtained with a single run of the STFT algorithm. The bottom one ($\alpha = 1$) locates the sinusoidal component at 50 Hz, but blurs the chirp component. On the contrary, the top one ($\alpha = 12.6$) locates the chirp component, but widens the sinusoidal component.This second Gaussian window, and the spectrogram that it generates, have been shifted to the frequency band [100 Hz-200 Hz].

Preprints (www.preprints.org) | NOT PEER-REVIEWED | Posted: 5 August 2019 doi:10.20944/preprints201908.0039.v1

Peer-reviewed version available at Energies 2019, 12, 3361; doi:10.3390/en12173361

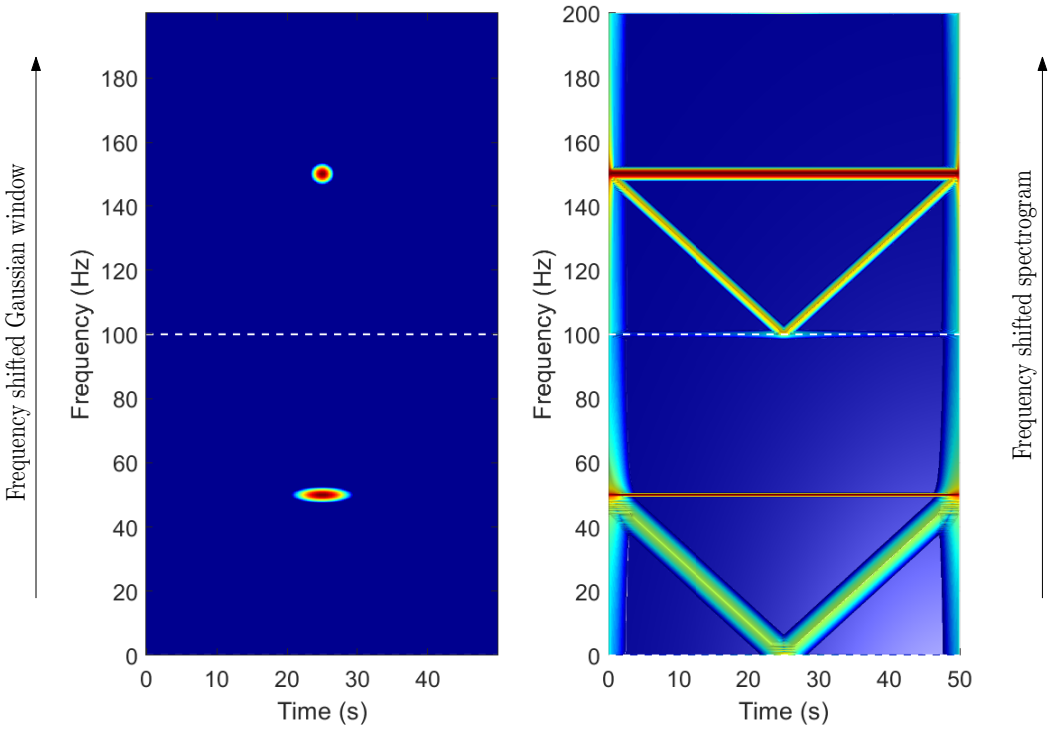

Figure 5. Spectrogram of the current signal (17) obtained in step 2 with the multi-band window (right). The Gaussian component of the window with $\alpha = 1$ (bottom, left) locates the sinusoidal component at 50 Hz (bottom, right), but fails to resolve the chirp component. On the contrary, the Gaussian component with $\alpha = 12.6$ (top, left), locates the chirp component, but widens the sinusoidal component (top, right).The Gaussian window that is frequency shifted (left) generates a spectrogram that is also frequency shift (right).

3. All the stacked, elementary spectrograms obtained in step 2 are shifted back to the frequency band [0-f_b], as shown in Fig. 6. This process has a negligible computational cost, just the renumbering of the frequency axis of each elementary spectrogram.

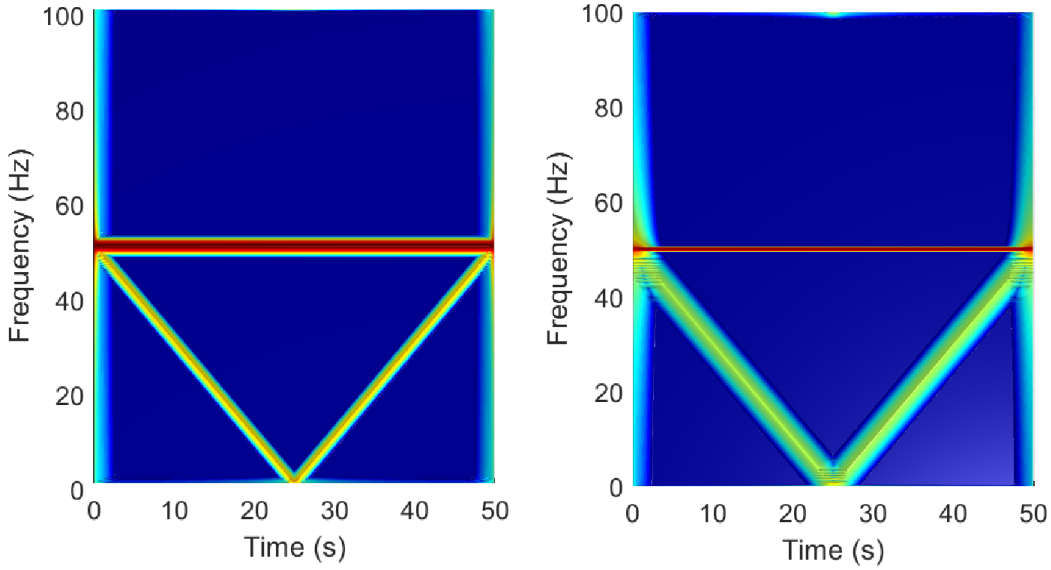

Figure 6. Relocation in the frequency axis of the elementary spectrograms, so that all of them span the same frequency band [0-f_b].

Preprints (www.preprints.org) | NOT PEER-REVIEWED | Posted: 5 August 2019 doi:10.20944/preprints201908.0039.v1

Peer-reviewed version available at Energies 2019, 12, 3361; doi:10.3390/en12173361

4. The points with the same time-frequency coordinates in all the relocated spectrograms obtained in step 3 (Fig. 6, are combined to give a single high resolution spectrogram of the TF region of diagnostic interest, in the frequency band [0 - f_b] (Fig. 7). The combination process used in this work consists in selecting, for each point of this region, the minimum value obtained among all the relocated spectrograms. The final result shows with a high resolution both the sinusoidal component at 50 Hz and the chirp component.

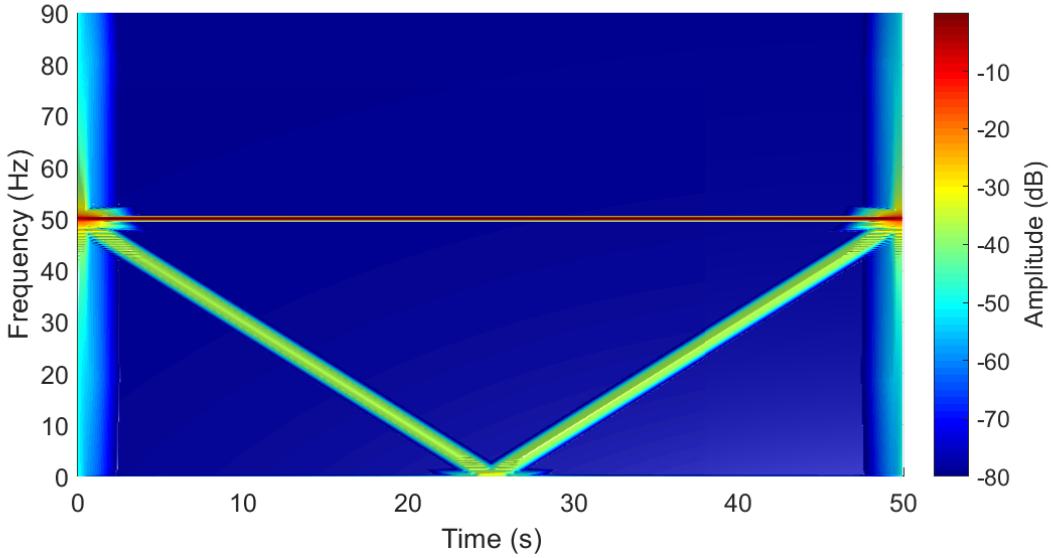

Figure 7. High resolution spectrogram of the current signal (17): for each point of the TF region of interest, the minimum value obtained among all the stacked spectrograms of Fig. 5, right, is selected. The final result shows with a high resolution both the sinusoidal component at 50 Hz and the chirp component.

4. Experimental Validation

For the experimental verification of the proposed approach, an IM whose characteristics are given in Appendix A has been prepared with a forced rotor fault, by drilling a hole in one of the rotor bars. The stator current during a startup transient has been acquired with a frequency rate $f_s = 5000$ Hz, during 12 seconds, using a current probe whose characteristics are given in Appendix B, and it is shown in Fig. 8.

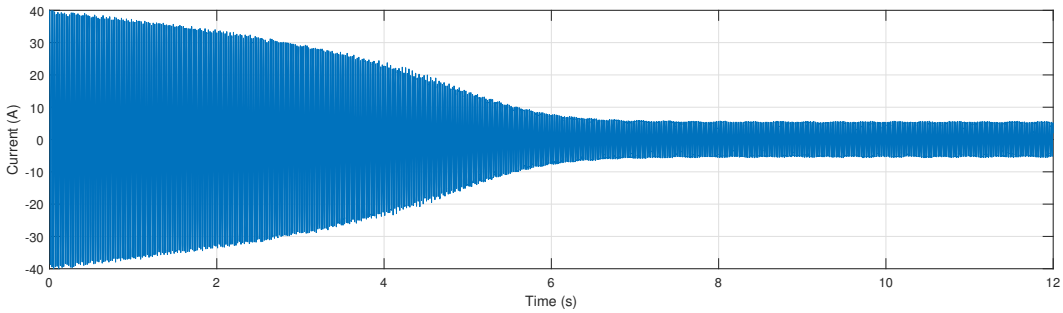

Figure 8. Start-up current of the motor of Appendix A with a broken bar fault.

From Table 1, the characteristic frequencies of the fault harmonics in an IM with a rotor asymmetry, such as a broken bar, are, for the main fault harmonics ($k/p = 1$ in Table 1),

$$f_{bb} = f_1(1 \pm 2s) \tag{19}$$

In particular, the fault harmonic with a frequency given by

$$f_{LSH} = f_1(1-2s), \tag{20}$$

which is known as the lower side-band harmonic (LSH), is commonly tracked for the diagnosis of rotor asymmetries. During a start-up transient, the trajectory of the LSH in the TF plane given by (20) generates a typical V-shaped fault signature [43], with a frequency that initially ($s = 1$) is equal to the fundamental frequency f_1, decreases to 0 ($s = 0.5$), and then increases again until its steady-state regime value of $f_1(1-2s) \approx f_1$, according to (20). The ability to detect this fault harmonic using the proposed method is to be assessed in this section.

The three steps presented in Section 3.1 will be followed in this experimental case to obtain the spectrogram of the current signal presented in Fig. 8.

1. The analysis window (15) is built:
   - first, the bandwidth of diagnostic interest is established. In this case, from (20), the frequency band of interest is the [0 - 50 Hz] band. Due to the presence of higher order harmonics in the current spectrum, apart form the LSH, a wider band [0 - 125 Hz] has been selected, in order to better assess the strength of the LSH compared with them. In this way, With a sampling frequency of 5000 Hz, the maximum number of elementary Gaussian windows from (14) is $Ng = 5000/125 = 40$ windows.
   - second, the parameter α_k of each of these windows in (15) is selected. In this case, a linear range of the parameter α is used, covering the range [$\alpha_{min} = 1$ - $\alpha_{max} = 700$].

The resulting multi-band window, applying (15), is

$$gm(t) = \sum_{k=0}^{39} \left(\frac{k\alpha_k}{\pi}\right)^{1/4} e^{-\frac{k\alpha_k}{2}t^2} e^{jk2\pi 125}, \tag{21}$$

with

$$\alpha_k = 1 + k\frac{700-1}{39} \quad k = 0, 1 \ldots 39. \tag{22}$$

The multi-band window (21) is displayed in Fig. 9, which shows the real (Fig. 9.top) and the imaginary part (Fig. 9.middle) of the window, as well as its spectrum (Fig. 9.bottom).

Preprints (www.preprints.org) | NOT PEER-REVIEWED | Posted: 5 August 2019 doi:10.20944/preprints201908.0039.v1

Peer-reviewed version available at Energies 2019, 12, 3361; doi:10.3390/en12173361

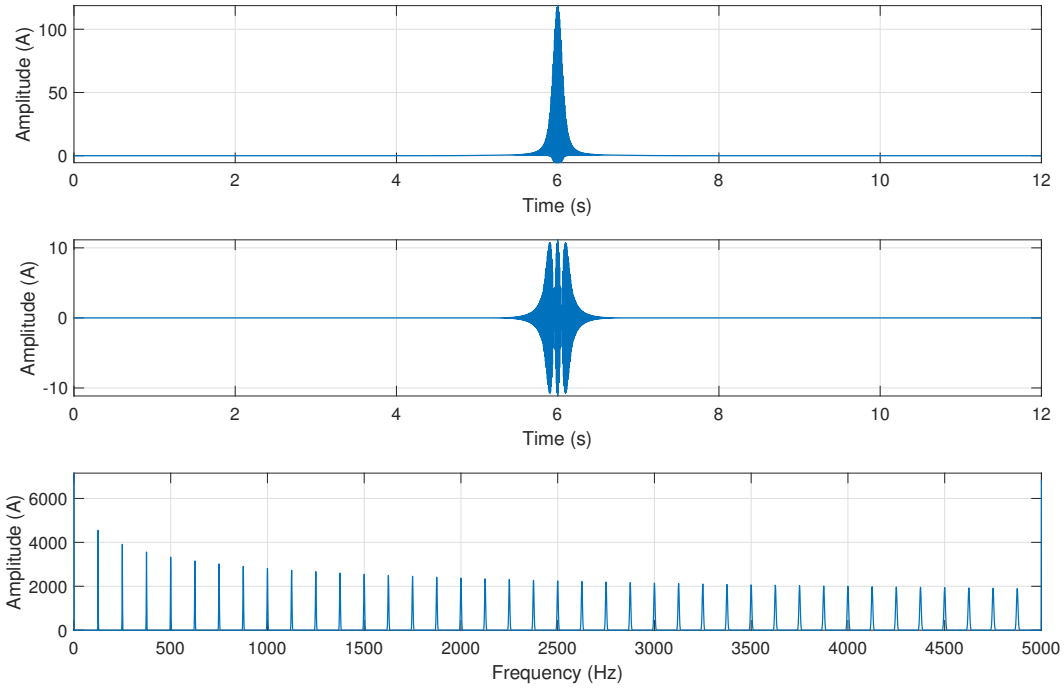

Figure 9. Multi-band window (21) in the time domain (real part, top, imaginary part, middle), and in the frequency domain (bottom). This windows contains 40 Gaussian windows, located in 40 adjacent frequency bands of 125 Hz, with values of α ranging from $\alpha_{min} = 1$ to $\alpha_{max} = 700$.

2. The spectrogram of the current signal of Fig. 8 is built. First, the current signal is low-pass filtered, keeping only the frequency bins of its spectrum lower than 125 Hz. After, and using the multi-band window (21) as sliding window, the STFT algorithm (4) is applied, which generates the spectrogram sown in Fig. 10. This spectrogram contains 40 elementary spectrograms in adjacent TF regions (Fig. 10, right), obtained with 40 different Gaussian windows (Fig. 10, left), at the cost of a single run of the STFT algorithm (6 seconds with the computer of Appendix C).

Preprints (www.preprints.org) | NOT PEER-REVIEWED | Posted: 5 August 2019 doi:10.20944/preprints201908.0039.v1

Peer-reviewed version available at Energies 2019, 12, 3361; doi:10.3390/en12173361

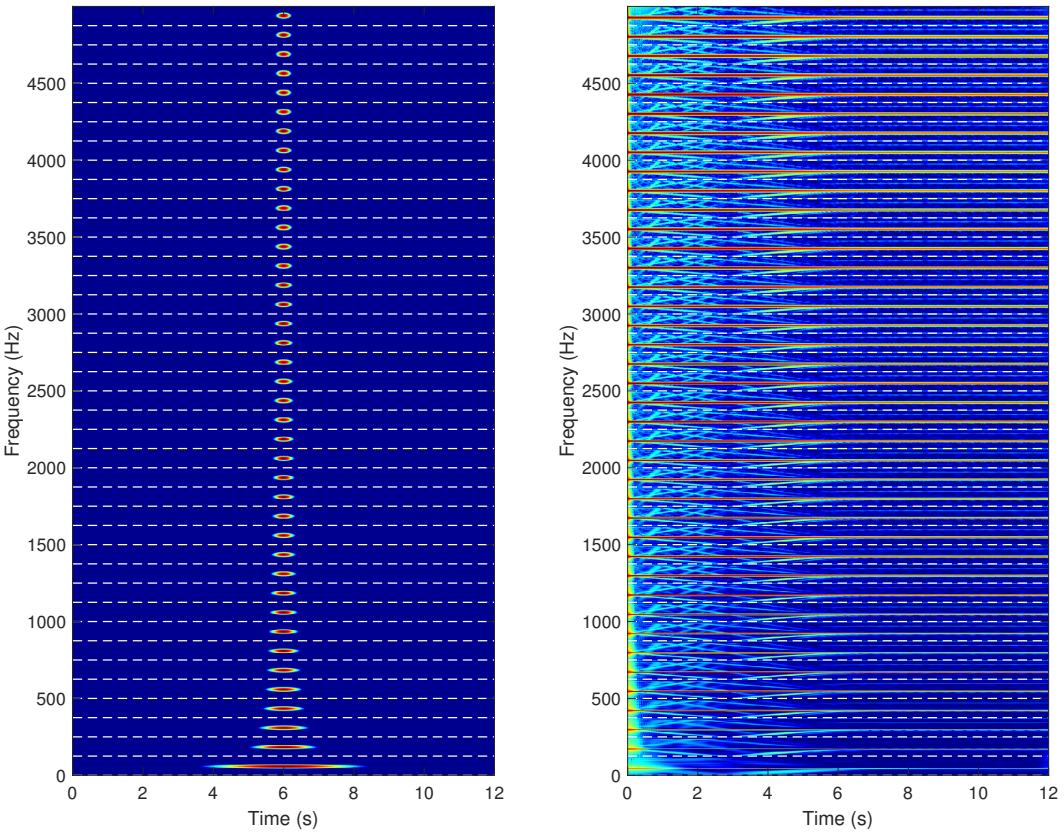

Figure 10. Spectrograms of the current of Fig. 8 (right) obtained with the multi-band window (21) (left). The 40 stacked spectrograms have been obtained with a single run of the STFT algorithm.

Two of the 40 individual Gaussian windows shown in Fig. 10 are displayed in Fig. 11, left, along with their corresponding current spectra (Fig. 11, right). The two zoomed bands corresponds to the spectrogram located in the base frequency band [0-125 Hz] (Fig. 11, bottom), which defines clearly the fundamental component, but blurs the fault harmonics, and to the spectrogram shifted to the frequency band [1500-1625 Hz], (Fig. 11, top) which defines clearly the fault harmonics, but widens the fundamental component.

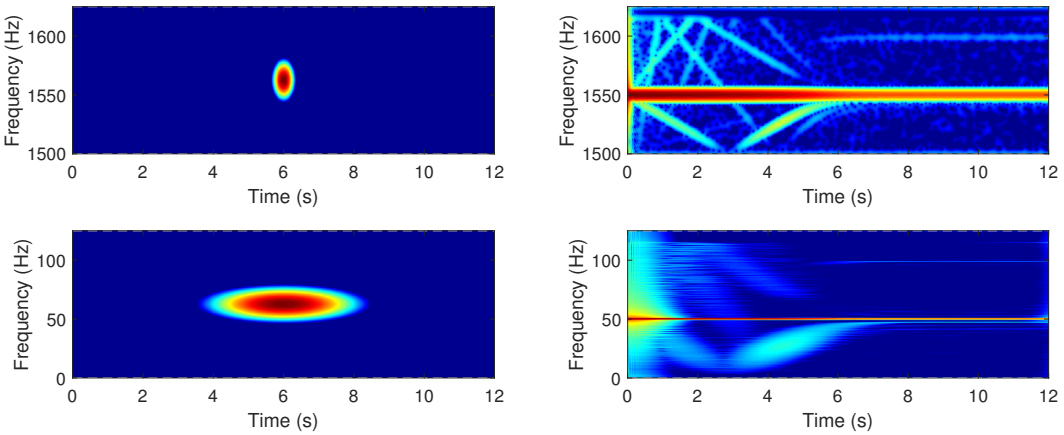

Figure 11. Zoom of Fig. 10 showing two of the individual Gaussian windows contained in the multi-band window of Fig. 10 (left), and the corresponding spectrograms generated with them (right). The two zoomed bands corresponds to the spectrogram located in base frequency band [0-125 Hz] (bottom), which defines clearly the fundamental component, but blurs the fault harmonics, and to the spectrogram shifted to the frequency band [1500-1625 Hz] (top), which defines clearly the fault harmonics, but widens the fundamental component.

3. All the stacked, elementary spectrograms obtained in step 2 (Fig. 10, right), are relocated in the base frequency band [0 125 Hz], by renumbering their frequency axis.
4. All the relocated, elementary spectrograms obtained in step 3 (Fig. 10, right), are combined to give a high resolution spectrogram of the TF region of diagnostic interest (Fig. 12). The combination process used in this work consists in selecting, for each point of this [0 - 125 Hz] region, the minimum value obtained among all the relocated spectrograms. The final result shows with a high resolution both the sinusoidal component at 50 Hz and the LSH fault component. Unlike the individual spectrograms, the optimized spectrogram clearly shows the LSH not only during the transient periode, but also when the steady state is reached; it is also remarkable the set of fault-related second-order components that are revealed, which helps to get a more reliable diagnostic.

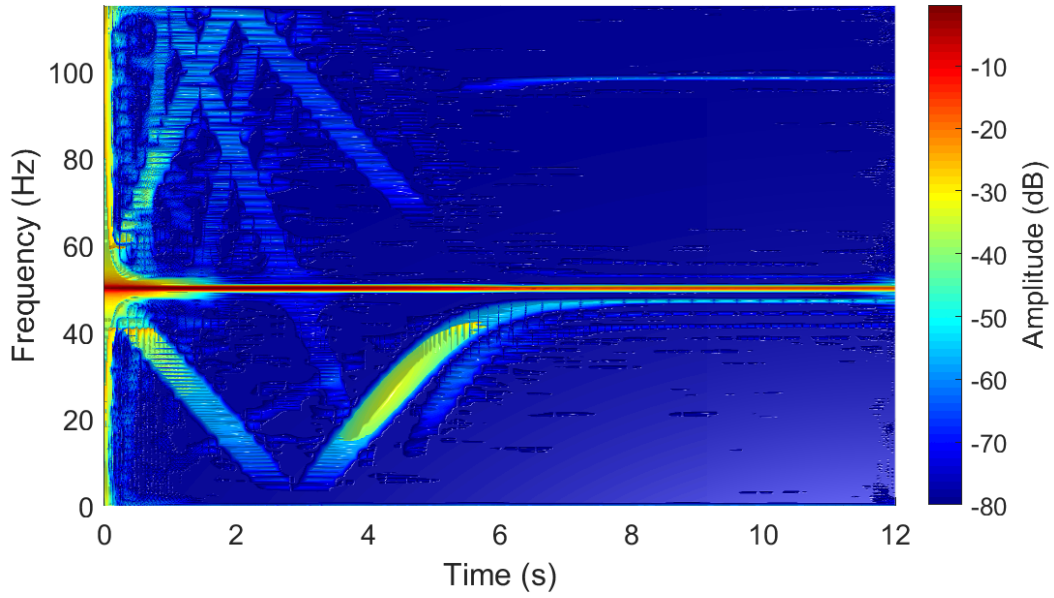

Figure 12. High resolution spectrogram of the current of Fig. 8: for each point of the TF region of interest, the minimum value obtained among all the stacked spectrograms of Fig. 10, right, is selected. The final result shows with a high resolution both the sinusoidal component at 50 Hz and the LSH fault component.

5. Conclusions

In this work, a novel technique for performing the fault diagnosis of IMs working in transient regime has been presented and validated experimentally. This technique consists in building a multi-band analysing window, composed by several, different Gaussian windows, stacked in the frequency domain. When this window is multiplied by the current signal in the time domain, it generates a spectrum which contains all the spectra generated by each of the Gaussian windows that form the multi-band window. In this way, a spectrogram containing even hundreds of different Gaussian windows can be obtained at the cost of a single run of the STFT algorithm. The selection of the parameters of the individual windows that compose the multi-band window can be setup by the user using different criteria, without affecting the performance of the proposed approach. In this work, a blind approach has been used, by selecting a range of individual windows that cover a wide range of, a priori, unkown fault harmonic components. This approach can be particularly useful for automated diagnostic system, which can operate without expert assistance, and for the detection of different types of faults. In this case, a single multi-band window can avoid the design of multiple analysis windows specifically designed for each single type fault.

Author Contributions: R.P. and A.S. developed the theoretical explanation of the method. J.B. and J.M. designed and carried out the experimental validations; M.P. wrote the paper and M.R. carried out the revision the paper.

Conflicts of Interest: The authors declare no conflict of interest.

Funding: This research was funded by the Spanish "Ministerio de Ciencia, Innovación y Universidades (MCIU)", the "Agencia Estatal de Investigación (AEI)" and the "Fondo Europeo de Desarrollo Regional (FEDER)" in the framework of the "Proyectos I+D+i - Retos Investigación 2018", project reference RTI2018-102175-B-I00 (MCIU/AEI/FEDER, UE).

Appendix A Motor Characteristics

Three-phase induction machine. Rated characteristics: $P = 1.1$ kW, $f = 50$ Hz, $U = 230/400$ V, $I = 2.7/4.6$ A, $n = 1410$ r/min , cos $\varphi = 0.8$.

Appendix B Current Clamp

Chauvin Arnoux MN60, Nominal measuring scope: 100 mA–20A, ratio input/output: 1 A/100 mV, intrinsic error: $\leq 2\% + 50$ mV, frequency use: 400 Hz–10 kHz.

Appendix C Computer Features

CPU: Intel Core i7-2600K CPU @ 3.40 GHZ RAM memory: 16 GB, Matlab Version: 9.6.0.1072779 (R2019a).

References

1. Chang, H.C.; Jheng, Y.M.; Kuo, C.C.; Hsueh, Y.M. Induction Motors Condition Monitoring System with Fault Diagnosis Using a Hybrid Approach. *Energies* **2019**, *12*.
2. Zhang, P.; Lu, D. A Survey of Condition Monitoring and Fault Diagnosis toward Integrated O&M for Wind Turbines. *Energies* **2019**, *12*.
3. Bandyopadhyay, I.; Purkait, P.; Koley, C. Performance of a Classifier Based on Time-Domain Features for Incipient Fault Detection in Inverter Drives. *IEEE Transactions on Industrial Informatics* **2019**, *15*, 3–14.
4. Artigao, E.; Honrubia-Escribano, A.; Gomez, E. In-Service Wind Turbine DFIG Diagnosis using Current Signature Analysis. *IEEE Transactions on Industrial Electronics* **2019**, pp. 1–1.
5. Swana, E.F.; Doorsamy, W. Investigation of Combined Electrical Modalities for Fault Diagnosis on a Wound-Rotor Induction Generator. *IEEE Access* **2019**, *7*, 32333–32342.
6. Esakimuthu Pandarakone, S.; Mizuno, Y.; Nakamura, H. A Comparative Study between Machine Learning Algorithm and Artificial Intelligence Neural Network in Detecting Minor Bearing Fault of Induction Motors. *Energies* **2019**, *12*.
7. Huang, B.; Feng, G.; Tang, X.; Gu, J.X.; Xu, G.; Cattley, R.; Gu, F.; Ball, A.D. A Performance Evaluation of Two Bispectrum Analysis Methods Applied to Electrical Current Signals for Monitoring Induction Motor-Driven Systems. *Energies* **2019**, *12*.
8. Bo, L.; Xu, G.; Liu, X.; Lin, J. Bearing Fault Diagnosis Based on Subband Time-Frequency Texture Tensor. *IEEE Access* **2019**, *7*, 37611–37619.
9. Yu, G. A Concentrated Time-Frequency Analysis Tool for Bearing Fault Diagnosis. *IEEE Transactions on Instrumentation and Measurement* **2019**, pp. 1–11.
10. Jiang, X.; Wang, J.; Shi, J.; Shen, C.; Huang, W.; Zhu, Z. A coarse-to-fine decomposing strategy of VMD for extraction of weak repetitive transients in fault diagnosis of rotating machines. *Mechanical Systems and Signal Processing* **2019**, *116*, 668–692.
11. Irhoumah, M.; Pusca, R.; Lefevre, E.; Mercier, D.; Romary, R. Detection of the Stator Winding Inter-Turn Faults in Asynchronous and Synchronous Machines Through the Correlation Between Harmonics of the Voltage of Two Magnetic Flux Sensors. *IEEE Transactions on Industry Applications* **2019**, *55*, 2682–2689.
12. Skowron, M.; Wolkiewicz, M.; Orlowska-Kowalska, T.; Kowalski, C.T. Effectiveness of Selected Neural Network Structures Based on Axial Flux Analysis in Stator and Rotor Winding Incipient Fault Detection of Inverter-fed Induction Motors. *Energies* **2019**, *12*.
13. Jia, Z.; Liu, Z.; Vong, C.M.; Pecht, M. A Rotating Machinery Fault Diagnosis Method Based on Feature Learning of Thermal Images. *IEEE Access* **2019**, *7*, 12348–12359.

14. B, P.S.; Hemamalini, S. Rational-Dilation Wavelet Transform based Torque Estimation from Acoustic signals for Fault Diagnosis in a Three Phase Induction Motor. *IEEE Transactions on Industrial Informatics* **2018**, pp. 1–1.
15. Glowacz, A.; Glowacz, W.; Glowacz, Z.; Kozik, J. Early fault diagnosis of bearing and stator faults of the single-phase induction motor using acoustic signals. *Measurement* **2018**, *113*, 1–9.
16. Tarchała, G.; Wolkiewicz, M. Performance of the Stator Winding Fault Diagnosis in Sensorless Induction Motor Drive. *Energies* **2019**, *12*.
17. Abdi Monfared, O.; Doroudi, A.; Darvishi, A. Diagnosis of rotor broken bars faults in squirrel cage induction motor using continuous wavelet transform. *COMPEL - The international journal for computation and mathematics in electrical and electronic engineering* **2019**, *38*, 167–182.
18. Nemec, M.; Ambrožič, V.; Fišer, R.; Nedeljković, D.; Drobnič, K. Induction Motor Broken Rotor Bar Detection Based on Rotor Flux Angle Monitoring. *Energies* **2019**, *12*.
19. Zappalá, D.; Sarma, N.; Djurović, S.; Crabtree, C.; Mohammad, A.; Tavner, P. Electrical & mechanical diagnostic indicators of wind turbine induction generator rotor faults. *Renewable Energy* **2019**, *131*, 14–24.
20. Salah, A.A.; Dorrell, D.G.; Guo, Y. A Review of the Monitoring and Damping Unbalanced Magnetic Pull in Induction Machines Due to Rotor Eccentricity. *IEEE Transactions on Industry Applications* **2019**, *55*, 2569 – 2580.
21. Wang, T.; Lu, G.; Yan, P. A Novel Statistical Time-Frequency Analysis for Rotating Machine Condition Monitoring. *IEEE Transactions on Industrial Electronics* **2019**, pp. 1–1.
22. Jiang, X.; Shi, J.; Huang, W.; Zhu, Z. Non-dominated solution set based on time–frequency infograms for local damage detection of rotating machines. *ISA Transactions* **2019**.
23. Faiz, J.; Moosavi, S. Eccentricity fault detection – From induction machines to DFIG—A review. *Renewable and Sustainable Energy Reviews* **2016**, *55*, 169–179.
24. Kumar, D.; Basit, A.; Saleem, A.; Abbas, E.G. PLC Based Monitoring & Protection of 3-Phase Induction Motors against Various Abnormal Conditions. 2019 2nd International Conference on Computing, Mathematics and Engineering Technologies (iCoMET). IEEE, 2019, pp. 1–6.
25. Guven, Y.; Atis, S. Implementation of an embedded system for real-time detection of rotor bar failures in induction motors. *ISA Transactions* **2018**, *81*, 210–221.
26. Garcia-Bracamonte, J.E.; Ramirez-Cortes, J.M.; de Jesus Rangel-Magdaleno, J.; Gomez-Gil, P.; Peregrina-Barreto, H.; Alarcon-Aquino, V. An Approach on MCSA-Based Fault Detection Using Independent Component Analysis and Neural Networks. *IEEE Transactions on Instrumentation and Measurement* **2019**, *68*, 1353–1361.
27. Pilloni, A.; Pisano, A.; Riera-Guasp, M.; Puche-Panadero, R.; Pineda-Sanchez, M. Fault Detection in Induction Motors. In *AC Electric Motors Control*; John Wiley & Sons Ltd, 2013; pp. 275–309.
28. Abd-el Malek, M.B.; Abdelsalam, A.K.; Hassan, O.E. Novel approach using Hilbert Transform for multiple broken rotor bars fault location detection for three phase induction motor. *ISA Transactions* **2018**, *80*, 439–457.
29. Burriel-Valencia, J.; Puche-Panadero, R.; Martinez-Roman, J.; Sapena-Bano, A.; Pineda-Sanchez, M.; Perez-Cruz, J.; Riera-Guasp, M.; Burriel-Valencia, J.; Puche-Panadero, R.; Martinez-Roman, J.; Sapena-Bano, A.; Pineda-Sanchez, M.; Perez-Cruz, J.; Riera-Guasp, M. Automatic Fault Diagnostic System for Induction Motors under Transient Regime Optimized with Expert Systems. *Electronics* **2018**, *8*, 6.
30. Rivera-Guillen, J.R.; De Santiago-Perez, J.; Amezquita-Sanchez, J.P.; Valtierra-Rodriguez, M.; Romero-Troncoso, R.J. Enhanced FFT-based method for incipient broken rotor bar detection in induction motors during the startup transient. *Measurement* **2018**, *124*, 277–285.
31. Burriel-Valencia, J.; Puche-Panadero, R.; Martinez-Roman, J.; Sapena-Bano, A.; Pineda-Sanchez, M. Short-Frequency Fourier Transform for Fault Diagnosis of Induction Machines Working in Transient Regime. *IEEE Transactions on Instrumentation and Measurement* **2017**, *66*, 432–440.
32. Shao, S.; McAleer, S.; Yan, R.; Baldi, P. Highly Accurate Machine Fault Diagnosis Using Deep Transfer Learning. *IEEE Transactions on Industrial Informatics* **2019**, *15*, 2446–2455.
33. Yang, B.; Liu, R.; Chen, X. Fault Diagnosis for a Wind Turbine Generator Bearing via Sparse Representation and Shift-Invariant K-SVD. *IEEE Transactions on Industrial Informatics* **2017**, *13*, 1321–1331.
34. Bo, L.; Xu, G.; Liu, X.; Lin, J. Bearing Fault Diagnosis Based on Subband Time-Frequency Texture Tensor. *IEEE Access* **2019**, *7*, 37611–37619.

35. Riera-Guasp, M.; Pineda-Sanchez, M.; Perez-Cruz, J.; Puche-Panadero, R.; Roger-Folch, J.; Antonino-Daviu, J.A. Diagnosis of Induction Motor Faults via Gabor Analysis of the Current in Transient Regime. *IEEE Transactions on Instrumentation and Measurement* **2012**, *61*, 1583–1596.
36. Fernandez-Cavero, V.; Morinigo-Sotelo, D.; Duque-Perez, O.; Pons-Llinares, J. A Comparison of Techniques for Fault Detection in Inverter-Fed Induction Motors in Transient Regime. *IEEE Access* **2017**, *5*, 8048–8063.
37. He, D.; Cao, H.; Wang, S.; Chen, X. Time-reassigned synchrosqueezing transform: The algorithm and its applications in mechanical signal processing. *Mechanical Systems and Signal Processing* **2019**, *117*, 255–279.
38. Yu, G.; Wang, Z.; Zhao, P.; Li, Z. Local maximum synchrosqueezing transform: An energy-concentrated time-frequency analysis tool. *Mechanical Systems and Signal Processing* **2019**, *117*, 537–552.
39. Ali, M.Z.; Shabbir, M.N.S.K.; Liang, X.; Zhang, Y.; Hu, T. Machine Learning based Fault Diagnosis for Single- and Multi-Faults in Induction Motors Using Measured Stator Currents and Vibration Signals. *IEEE Transactions on Industry Applications* **2019**, *55*, 2378 – 2391.
40. Qin, Y.; Zou, J.; Tang, B.; Wang, Y.; Chen, H. Transient feature extraction by the improved orthogonal matching pursuit and K-SVD algorithm with adaptive transient dictionary. *IEEE Transactions on Industrial Informatics* **2019**, pp. 1–1.
41. Gabor, D. Theory of communication. Part 1: The analysis of information. *Journal of the Institution of Electrical Engineers - Part III: Radio and Communication Engineering* **1946**, *93*, 429–441(12).
42. Sapena-Bano, A.; Pineda-Sanchez, M.; Puche-Panadero, R.; Martinez-Roman, J.; Matic, D. Fault Diagnosis of Rotating Electrical Machines in Transient Regime Using a Single Stator Current's FFT. *IEEE Transactions on Instrumentation and Measurement* **2015**, *64*, 3137–3146.
43. Burriel-Valencia, J.; Puche-Panadero, R.; Martinez-Roman, J.; Sapena-Bano, A.; Pineda-Sanchez, M. Fault Diagnosis of Induction Machines in a Transient Regime Using Current Sensors with an Optimized Slepian Window. *Sensors* **2018**, *18*.